Gust Load Alleviation and Ride Quality Improvement with Incremental Nonlinear Dynamic Inversion

Wang, Xiaotian; van Kampen, Erik-Jan; Chu, QP

DOI
10.2514/6.2017-1400

Publication date
2017

Document Version
Accepted author manuscript

Published in
Proceedings of the AIAA atmospheric flight mechanics conference

This is an Accepted Manuscript of an article published in: AIAA atmospheric flight mechanics conference, 9/01/17 - 13/01/17 Grapevine, USA ISBN: 978-1-62410-390-2
Available online: https://arc.aiaa.org/doi/10.2514/6.2017-1400

Gust Load Alleviation and Ride Quality Improvement with Incremental Nonlinear Dynamic Inversion

X. Wang*, E. van Kampen †, Q.P.Chu ‡

Delft University of Technology, Delft, Zuid-Holland, 2629HS, The Netherlands

In this paper, a non-cascaded control framework of Incremental Nonlinear Dynamic Inversion (INDI) is proposed to alleviate gust loads and improve ride quality using direct lift control. By feeding back linear and angular accelerations, the dependency of the control laws on model has been reduced, which enhances the robust performance of the system. Simulations of a quasi-rigid aircraft flying through various spatial turbulence and gust fields demonstrate the feasibility of the proposed INDI gust load alleviation (GLA) controller. Furthermore, a cascaded automatic flight control system is designed based on the INDI GLA control law. Desired tracking performance and load alleviation can be achieved simultaneously. Additionally, a comparison with LQR/LQG control is presented from the perspective of GLA performance, command tracking, and robustness.

I. Introduction

Atmospheric flight can be very unpleasant due to turbulence and gusts disturbances. The bumpiness and structural vibrations caused by turbulence and gusts can lead to structural fatigue, degrade handling qualities, impair passenger comfort and even threaten flight safety. Apart from passive gust load alleviation (GLA) technologies such as using bend-twist coupling of composite beams, active GLA control also provides a promising approach.

Before designing active GLA control laws, one should first know the effects of gust and turbulence on the aircraft. Three questions arise when modelling these effects. First of all, how to describe the gust and turbulence fields either in the time, frequency or spatial domain? Following this is the aerodynamic problem of how to calculate the aerodynamic force and moment increments caused by gust and turbulence fields? Finally, how to set up a high fidelity model integrating flight dynamics, structural vibration dynamics and aerodynamics to simulate the aircraft dynamic response to incremental force and moment excitations?

Formulated by nonlinear ordinary differential equations and a series of second-order linear differential equations respectively, flight dynamics and aeroelasticity were treated as different disciplines. However, with the wide usage of composite materials, the couplings between rigid body maneuvering dynamics and structural vibrations are increasingly significant for large transport aircrafts. The mean axes method was introduced by Schmidt[1] to avoid inertia coupling, but the constraints defining these axes are tedious to enforce, prevalent practice is using mean axes without satisfying constraints nor expressing aerodynamic forces along mean axes, which leads to controversial results.[2] Meirovitch[2] derived the coupled flight dynamics and aeroelasticity equations in quasi-coordinates. These equations encompass both inertia and aerodynamic couplings effects, and will be used for the GLA control design in present paper.

When nonlinear flight dynamic equations are coupled with high order linear structural vibration equations, the resulting equations of motion (EQM) are nonlinear and of high dimension. Linearizing the coupled EQM on preselected trimming points, and applying the linear control methods is a common practice,[2–4] which however, requires the gain scheduling technique when multiple operation points are considered. The parameter tuning and interpolation process of gain scheduling method can be tedious.

*PhD Candidate, Control and Simulation Section, Faculty of Aerospace Engineering, Delft University of Technology; Kluyverweg 1, 2629HS, Delft, The Netherlands. X.Wang-6@tudelft.nl.

†Assistant Professor, Control and Simulation Section, Faculty of Aerospace Engineering, Delft University of Technology; Kluyverweg 1, 2629HS, Delft, The Netherlands, E.vanKampen@tudelft.nl, AIAA member.

‡Associate Professor, Control and Simulation Section, Faculty of Aerospace Engineering, Delft University of Technology; Kluyverweg 1, 2629HS, Delft, The Netherlands, Q.P.Chu@tudelft.nl, AIAA member.

Various sensors, effectors,[5] and control laws (LQG,[4] robust,[6] adaptive feedforward,[7] model predictive,[8] etc.) have been used and tested.[9] No single control law synthesis technique or methodology has been proven superior, although many of them have been demonstrated successfully. Since all these controllers are model based approaches, control performance is affected by limited model knowledge. Therefore, control laws that provide robustness in the presence of inaccuracies while coping with system nonlinearities are anticipated. Until recently, only so-called adaptive control methods provide the level of robustness for GLA problems. These methods, in some form or the other, rely on online identification of the aircraft dynamic behaviour and adaptation of control laws if necessary. Online identification unfortunately requires high computing power and so far, the parameter convergence property of online identification is not quick and smooth enough to handle the GLA problem. Besides, the additional excitations for online model identification purposes may aggravate vibrations. Furthermore, online system identification based adaptive control laws are indirect and modular adaptive controls, whose stability cannot be guaranteed due to the separation between model identification and control law designs.

In view of the deficiencies of adaptive control, the novel Incremental Nonlinear Dynamic Inversion (INDI) control method was proposed to enhance robustness.[10,11] Based on the time scale separation principle of physical systems, the original uncertain system can be greatly simplified due to the rich information gathered in state derivatives (linear and angular accelerations). The unknown system is reduced to a partially certain and linear system with an incremental input. Controlling this system becomes therefore feasible without applying any complex adaptive or intelligent control algorithms. This weakens the dependency of the control laws on model information and thus on online identification. In fact, the only model information explicitly required is the effectiveness of all the available controls, although the robustness of the closed-loop system to the control effectiveness matrix uncertainties is high from both theoretical analysis and unmanned aircraft flight tests.[10,12]

In this paper, we present three main contributions: 1) An INDI GLA control law designed to alleviate gust loads and improve ride quality. Different from existing INDI applications, the INDI GLA control law uses direct lift control with a non-cascaded structure. Also, a more general case where the center of gravity (c.g.) deviates from the body axes origin is investigated. Besides, control allocation is achieved for a traditional aircraft configuration using INDI. 2) An INDI automatic flight control law which allows alleviating loads while tracking flight control commands. 3) A comparison of presented INDI control law with LQR/LQG control. Being a linear controller, the widely used LQR/LQG control requires gain-scheduling in wider flight envelop. Also, the cost function of LQR/LQG control is designed beforehand aiming at a specific target. Improved global and task applicability are expected for INDI control. The GLA and command tracking performance of LQR/LQG control will also be compared to the present INDI control.

This paper is organized as follows: Sec. II sets up the EQM of the quasi-rigid aircraft. Turbulence/gust descriptions and incremental forces calculations are presented in Sec. III. Sec. IV derives the INDI GLA laws with the resulting simulation results shown and discussed in Sec. V. In Sec. VI, INDI control is compared to LQR control from different perspectives. Main conclusions are drawn in Sec. VII.

II. Quasi-rigid Aircraft Equations of Motion

The EQM of the quasi-rigid aircraft is simplified from Meirovitch's unified flexible aircraft model.[2] By setting all the elastic displacements and velocities into zero, the quasi-rigid aircraft EQM in quasi-coordinates can be expressed as

$$\begin{bmatrix} \dot{\mathbf{R}}_f \\ \dot{\boldsymbol{\theta}}_f \\ \dot{\mathbf{p}}_{V_f} \\ \dot{\mathbf{p}}_{\omega_f} \end{bmatrix} = \begin{bmatrix} C_{bi}^T \mathbf{V}_f \\ E_f^{-1} \boldsymbol{\omega}_f \\ -\tilde{\omega}_f \mathbf{p}_{V_f} + \mathbf{F} \\ -\tilde{V}_f \mathbf{p}_{V_f} - \tilde{\omega}_f \mathbf{p}_{\omega_f} + \mathbf{M} \end{bmatrix} \tag{1}$$

In which $\mathbf{R}_f$ and $\boldsymbol{\theta}_f$ indicate the position and Euler angles of the quasi-coordinates $x_f y_f z_f$ with respect to inertia axes $X_E Y_E Z_E$, while $\mathbf{V}_f$ and $\boldsymbol{\omega}_f$ represent the translational and rotational velocities of the $x_f y_f z_f$ axes. $\mathbf{p}_{V_f}$ and $\mathbf{p}_{\omega_f}$ indicate the linear and angular momenta of the aircraft. $C_{bi}(\phi, \theta, \psi)$ is the rotation transformation matrix from inertial axes $X_E Y_E Z_E$ to $x_f y_f z_f$, and the $E_f(\phi, \theta)$ matrix transforms Eulerian velocities $\dot{\boldsymbol{\theta}}_f$ to angular velocities $\boldsymbol{\omega}_f$. Bold mark indicates a vector and $(\tilde{\cdot})$ refers to its corresponding skew-symmetric matrix. $\mathbf{F}$ and $\mathbf{M}$ are the total forces and moments. The momenta and velocities are linked by

system mass matrix as shown in Eq. (2).

$$\begin{bmatrix} \mathbf{p}_{V_f} \\ \mathbf{p}_{\omega_f} \end{bmatrix} = \begin{bmatrix} mI & \tilde{S}^T \\ \tilde{S} & J \end{bmatrix} \begin{bmatrix} \mathbf{V}_f \\ \boldsymbol{\omega}_f \end{bmatrix} \tag{2}$$

In which m and J represent the mass and the moment of inertia of the aircraft respectively. The origin of quasi-coordinate is not necessarily on the c.g., leading to the coupled translational and rotational motion, reflected by the skew-symmetric matrix of the first moment of area $\tilde{S}$.

III. Gust and Turbulence Effects on the Aircraft

A. Gust and Turbulence Models

Atmospheric disturbances can be considered as a superposition of mean wind, waves and turbulence.[13] With the time scale of hours and tens of minutes respectively, mean wind and waves are primarily of importance to navigation problems. Deterministic discrete gust and stochastic continuous turbulence are on the orders of seconds to minutes, which have significant influence on aircraft dynamic response. Compared to Dryden spectrum for continuous turbulence, the von Kármán spectrum better fits available theoretical and experimental data especially in high frequency range,[14] but its irrational spectrum requires approximate difference equations to generate turbulence velocities in the time domain. An alternative approach is to realize a von Kármán spectrum in the spatial domain. Its energy function and corresponding spectral tensor are expressed as[14,15]

$$E(k) = \frac{110}{9}\sigma^2 L_g \frac{(2\pi a L_g k)^4}{[1+(2\pi a L_g k)^2]^{17/6}}, \quad \Phi_{ij}(k) = \frac{E(k)}{4\pi k^4}(k^2\delta_{ij} - k_i k_j) \tag{3}$$

In which $k = \sqrt{{k_1}^2 + {k_2}^2 + {k_3}^2}$ represents the spatial frequency norm, constant a equals to 1.339, L_g and σ^2 refer to the turbulence length scale and variance respectively. With the relation $\Omega = 2\pi k$, the vertical turbulence auto spectrum in non-dimensional spatial frequency form is shown as[14]

$$S_{w_g w_g}(\Omega_x L_g, \Omega_y L_g) = \frac{4\sigma^2 a^2}{9\pi} \frac{(a\Omega_x L_g)^2 + (a\Omega_y L_g)^2}{[1+(a\Omega_x L_g)^2 + (a\Omega_x L_g)^2]^{7/3}} \tag{4}$$

For a specific two dimensional (2D) uncorrelated vertical turbulence field, the vertical velocity component $w_g(\frac{X_E}{L_g}, \frac{Y_E}{L_g})$ in the time domain is obtained by 2D Fourier transform as

$$w_g(\frac{X_E}{L_g}, \frac{Y_E}{L_g}) = \mathscr{F}^{-2}\{\sqrt{S_{w_g w_g}(\Omega_x L_g, \Omega_y L_g)} \frac{\mathscr{F}^2\{w_n(\frac{X_E}{L_g}, \frac{Y_E}{L_g})\}}{\sqrt{\frac{\Delta X_E}{L_g}}\sqrt{\frac{\Delta Y_E}{L_g}}}\} \tag{5}$$

where $w_n(\frac{X_E}{L_g}, \frac{Y_E}{L_g})$ represents the 2D non-dimensional spatial domain Gauss white noise, which is divided by the spatial sampling frequency $\sqrt{\frac{\Delta X_E}{L_g}}, \sqrt{\frac{\Delta Y_E}{L_g}}$ to maintain unity energy. In this paper, the turbulence field is generated with scale length $L_g = 762m$ and standard derivation $\sigma = 3m/s$. The spatial sampling frequency is chosen as $\frac{\Delta X_E}{L_g} = \frac{\Delta Y_E}{L_g} = 0.001$, the resulting gust field is shown in Fig. 1, which can be verified by comparing the covariance function of the simulated field with theoretical values.

Compared to sharp-edged and ramped gust models, the "1-cos" gust model can more precisely capture the solitary gust feature and is adopted in the Federal Aviation Regulation. A "1-cos" gust is defined as Eq. (6) and can be broadened into symmetric w_{g_s} and asymmetric w_{g_a} gust field as described by Eq. (7).

$$w_g = \frac{w_m}{2}(1 - \cos\frac{2\pi X_E}{\lambda_x}) \tag{6}$$

$$w_{g_s} = \frac{w_m}{4}(1 - \cos\frac{2\pi X_E}{\lambda_x})(1 - \cos\frac{2\pi Y_E}{\lambda_y}), \qquad w_{g_a} = \frac{w_m}{2}(1 - \cos\frac{2\pi X_E}{\lambda_x})\sin\frac{2\pi Y_E}{\lambda_y} \tag{7}$$

In which w_m represents the maximum gust velocity and λ_x, λ_y refer to the gust lengths in X_E, Y_E directions. An example of variant symmetric and asymmetric gust field is given in Fig. 2, in which $w_{g_1}(\lambda_x = \lambda_y = 100m, w_m = 5m/s)$ and $w_{g_2}(\lambda_x = \lambda_y = 180m, w_m = 5m/s)$ represent symmetric gusts, while $w_{g_3}(\lambda_x = \lambda_y = 80m, w_m = 6m/s)$ and $w_{g_4}(\lambda_x = \lambda_y = 120m, w_m = 8m/s)$ represent asymmetric gusts.

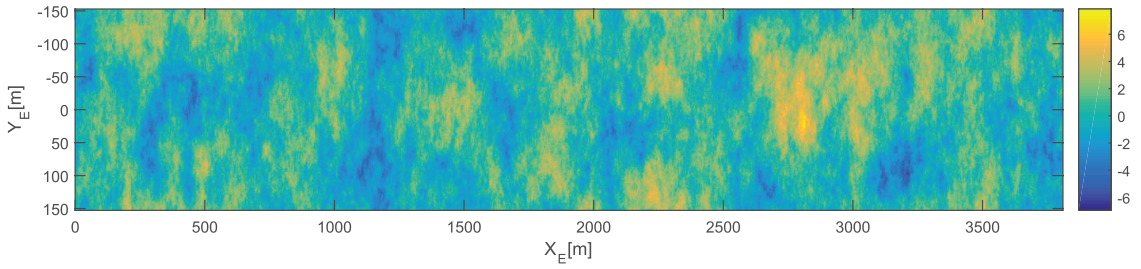

Figure 1. 2D von Kármán vertical turbulence field with $L_g = 762m, \sigma = 3m/s$.

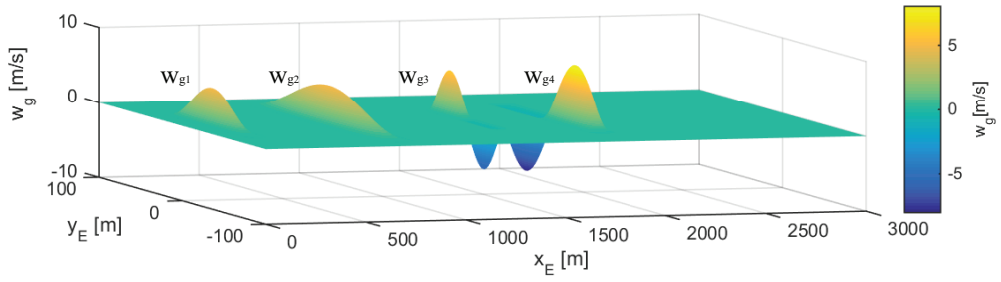

Figure 2. 2D "1-cos" vertical gust field.

B. Aircraft Response to Gust and Turbulence

The choice of model for the aerodynamic effects of gust fields is governed by the emphasis of the problem. For investigation of navigation, rigid body mode control and handling quality problems, quasi-steady aerodynamics and relatively rough gust field descriptions are often used. The linear gust field description models the gust velocities on the c.g. as well as the gust gradients around it, represented by $g = [u_g, v_g, w_g, p_g, q_g, r_{1g}, r_{2g}]$.[16] The linear gust field description, however, exaggerates the linear gradient effect at high wave number. Etkin's four point aircraft (FPA) model is proposed to avoid the truncation of high frequency response spectra. Regarding the FPA method, the gust-induced aerodynamic force and moment coefficients can be expanded as polynomial functions of gust derivatives (as a function of stability derivatives), making it easy to incorporate gust effects in aircraft EQM.

When significant structural dynamics are involved, unsteady aerodynamics, which is frequency depended, should be used to calculate the aeroelastic dynamic loads. The existing unsteady aerodynamic modeling methods for dynamic load calculations include 2D unsteady airfoil theory, the doublet lattice method (DLM), the unsteady vortex lattice method (UVLM), and the computational fluid dynamics method (CFD). Written in time domain, the UVLM method allows direct computation of the transient aerodynamic responses. The newly developed 3D continuous-time state-space unsteady aerodynamic modeling method[17] provides an efficient way for unsteady aerodynamic analysis.

The reduced frequencies of rigid aircraft modes are low, so quasi-steady aerodynamics is used in present model. Strip theory is applied and the turbulence/gust induced local velocities are calculated by interpolating the spatial turbulence/gust fields at the aerodynamic center of each strip (as shown by Fig. 3).

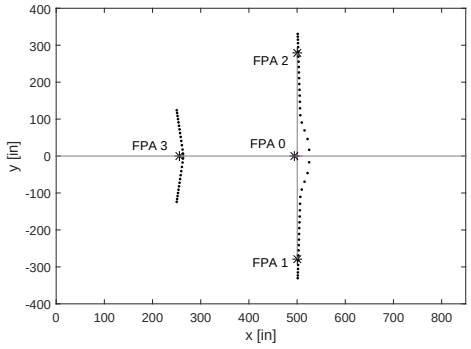

Figure 3. Interpolation points (dots) for local turbulence/gust velocities.

IV. Incremental Nonlinear Dynamic Inversion (INDI) Application

A. INDI GLA Control Law

In this section, the INDI GLA control law will be designed for a quasi-rigid aircraft. Considering the dynamic part of the quasi-rigid aircraft EQM, Eq. (1) can be rewritten as

$$\begin{bmatrix} \frac{\delta \mathbf{V}_f}{\delta t} \\ \frac{\delta \boldsymbol{\omega}_f}{\delta t} \end{bmatrix} = \begin{bmatrix} mI & \tilde{S}^T \\ \tilde{S} & J \end{bmatrix}^{-1} \begin{bmatrix} -\tilde{\omega}_f m I \mathbf{V}_f - \tilde{\omega}_f \tilde{S}^T \boldsymbol{\omega}_f + \mathbf{F} \\ -\tilde{V}_f \tilde{S}^T \boldsymbol{\omega}_f - \tilde{\omega}_f \tilde{S} \mathbf{V}_f - \tilde{\omega}_f J \boldsymbol{\omega}_f + \mathbf{M} \end{bmatrix} \tag{8}$$

Define $\mathbf{i}, \mathbf{j}, \mathbf{k}$ as the unit vectors of quasi-coordinates $x_f y_f z_f$, then $\mathbf{V}_f = V_x \mathbf{i} + V_y \mathbf{j} + V_z \mathbf{k}$. The absolute acceleration $\frac{d\mathbf{V}_f}{dt}$ and the relative acceleration $\frac{\delta \mathbf{V}_f}{\delta t}$ expressed in the body frame $x_f y_f z_f$ can be given as

$$\begin{aligned} \frac{d\mathbf{V}_f}{dt} &= \frac{\delta \mathbf{V}_f}{\delta t} + \boldsymbol{\omega}_f \times \mathbf{V}_f \\ \frac{\delta \mathbf{V}_f}{\delta t} &= \frac{dV_x}{dt}\mathbf{i} + \frac{dV_y}{dt}\mathbf{j} + \frac{dV_z}{dt}\mathbf{k} = \dot{V}_x \mathbf{i} + \dot{V}_y \mathbf{j} + \dot{V}_z \mathbf{k} \end{aligned} \tag{9}$$

Writing the inversion of mass matrix as

$$\begin{bmatrix} mI & \tilde{S}^T \\ \tilde{S} & J \end{bmatrix}^{-1} = \begin{bmatrix} m_{11} & m_{12} \\ m_{21} & m_{22} \end{bmatrix} \tag{10}$$

Then

$$\begin{aligned} \begin{bmatrix} \frac{\delta \mathbf{V}_f}{\delta t} \\ \frac{\delta \boldsymbol{\omega}_f}{\delta t} \end{bmatrix} &= \begin{bmatrix} m_{11}(-\tilde{\omega}_f m I \mathbf{V}_f - \tilde{\omega}_f \tilde{S}^T \boldsymbol{\omega}_f + \mathbf{F}) + m_{12}(-\tilde{V}_f \tilde{S}^T \boldsymbol{\omega}_f - \tilde{\omega}_f \tilde{S} \mathbf{V}_f - \tilde{\omega}_f J \boldsymbol{\omega}_f + \mathbf{M}) \\ m_{21}(-\tilde{\omega}_f m I \mathbf{V}_f - \tilde{\omega}_f \tilde{S}^T \boldsymbol{\omega}_f + \mathbf{F}) + m_{22}(-\tilde{V}_f \tilde{S}^T \boldsymbol{\omega}_f - \tilde{\omega}_f \tilde{S} \mathbf{V}_f - \tilde{\omega}_f J \boldsymbol{\omega}_f + \mathbf{M}) \end{bmatrix} \\ &\triangleq \begin{bmatrix} \boldsymbol{\Gamma}(\mathbf{V}_f, \boldsymbol{\omega}_f) + m_{11}\mathbf{F} + m_{12}\mathbf{M} \\ \boldsymbol{\Upsilon}(\mathbf{V}_f, \boldsymbol{\omega}_f) + m_{21}\mathbf{F} + m_{22}\mathbf{M} \end{bmatrix} \end{aligned} \tag{11}$$

The forces and moments can be classified as aerodynamic $(\mathbf{F}_a, \mathbf{M}_a)$, gravity $(\mathbf{F}_G, \mathbf{M}_G)$, and control $(\mathbf{F}_c, \mathbf{M}_c)$ forces and moments formulated as

$$\begin{aligned} \mathbf{F}(\mathbf{V}_f, \boldsymbol{\omega}_f, \boldsymbol{\delta}, \boldsymbol{\theta}_f) &= \mathbf{F}_a(\mathbf{V}_f, \boldsymbol{\omega}_f) + \mathbf{F}_G(\boldsymbol{\theta}_f) + \mathbf{F}_c(\delta_{a_s}, \delta_{a_a}, \delta_e, \delta_r, \delta_p) \\ \mathbf{M}(\mathbf{V}_f, \boldsymbol{\omega}_f, \boldsymbol{\delta}, \boldsymbol{\theta}_f) &= \mathbf{M}_a(\mathbf{V}_f, \boldsymbol{\omega}_f) + \mathbf{M}_G(\boldsymbol{\theta}_f) + \mathbf{M}_c(\delta_{a_s}, \delta_{a_a}, \delta_e, \delta_r, \delta_p) \end{aligned} \tag{12}$$

In the above equations, δ_{a_s} and δ_{a_a} represent the symmetric and asymmetric aileron deflections respectively. $\mathbf{M}_G$ is relevant to $\boldsymbol{\theta}_f$ because the origin of the quasi-coordinates is not necessarily on the c.g. Eq. (11) is then expanded into first order Taylor series around the current states and control inputs (denoted by

subscript 0) to obtain the incremental form as

$$\begin{aligned}
\frac{\delta \mathbf{V}_f}{\delta t} &\approx \left.\frac{\delta \mathbf{V}_f}{\delta t}\right|_0 + \left.\frac{\partial(\mathbf{\Gamma}(\mathbf{V}_f,\boldsymbol{\omega}_f)+m_{11}\mathbf{F}_a+m_{12}\mathbf{M}_a)}{\partial \mathbf{V}_f}\right|_0 \Delta\mathbf{V}_f + \left.\frac{\partial(\mathbf{\Gamma}(\mathbf{V}_f,\boldsymbol{\omega}_f)+m_{11}\mathbf{F}_a+m_{12}\mathbf{M}_a)}{\partial \boldsymbol{\omega}_f}\right|_0 \Delta\boldsymbol{\omega}_f \\
&+ \left.\frac{\partial(m_{11}\mathbf{F}_G+m_{12}\mathbf{M}_G)}{\partial \boldsymbol{\theta}_f}\right|_0 \Delta\boldsymbol{\theta}_f + \left.\frac{\partial(m_{11}\mathbf{F}_c+m_{12}\mathbf{M}_c)}{\partial \boldsymbol{\delta}}\right|_0 \Delta\boldsymbol{\delta} \triangleq \left.\frac{\delta \mathbf{V}_f}{\delta t}\right|_0 + \mathbf{K}_V + \mathbf{K}_\omega + \mathbf{K}_\theta + \mathbf{K}_\delta \\
\frac{\delta \boldsymbol{\omega}_f}{\delta t} &\approx \left.\frac{\delta \boldsymbol{\omega}_f}{\delta t}\right|_0 + \left.\frac{\partial(\mathbf{\Upsilon}(\mathbf{V}_f,\boldsymbol{\omega}_f)+m_{21}\mathbf{F}_a+m_{22}\mathbf{M}_a)}{\partial \mathbf{V}_f}\right|_0 \Delta\mathbf{V}_f + \left.\frac{\partial(\mathbf{\Upsilon}(\mathbf{V}_f,\boldsymbol{\omega}_f)+m_{21}\mathbf{F}_a+m_{22}\mathbf{M}_a)}{\partial \boldsymbol{\omega}_f}\right|_0 \Delta\boldsymbol{\omega}_f \\
&+ \left.\frac{\partial(m_{21}\mathbf{F}_G+m_{22}\mathbf{M}_G)}{\partial \boldsymbol{\theta}_f}\right|_0 \Delta\boldsymbol{\theta}_f + \left.\frac{\partial(m_{21}\mathbf{F}_c+m_{22}\mathbf{M}_c)}{\partial \boldsymbol{\delta}}\right|_0 \Delta\boldsymbol{\delta} \\
&\triangleq \left.\frac{\delta \boldsymbol{\omega}_f}{\delta t}\right|_0 + \mathbf{W}_V + \mathbf{W}_\omega + \mathbf{W}_\theta + \mathbf{W}_\delta
\end{aligned} \tag{13}$$

For simplicity, items related to $\Delta\mathbf{V}_f, \Delta\boldsymbol{\omega}_f, \Delta\boldsymbol{\theta}_f, \Delta\boldsymbol{\delta}$ in the translational equation are represented by $\mathbf{K}_V, \mathbf{K}_\omega, \mathbf{K}_\theta, \mathbf{K}_\delta$, and are represented by $\mathbf{W}_V, \mathbf{W}_\omega, \mathbf{W}_\theta, \mathbf{W}_\delta$ in the rotational equation. Eq. (13) can be simplified into Eq. (14) when noticing that for an incremental time step (high sampling frequency), the variations in $\mathbf{K}_V, \mathbf{K}_\omega, \mathbf{K}_\theta, \mathbf{W}_V, \mathbf{W}_\omega, \mathbf{W}_\theta$ are much smaller than those in $\mathbf{K}_\delta, \mathbf{W}_\delta$. This can be explained by the physical principle of control surfaces, whose deflection will change moments and forces, leading to changes of angular and linear accelerations as a direct effect. Following this, the changes in angular rates, velocities and attitudes will gradually accumulate over time. The item values in Eq. (13) will be compared numerically in Sec. V.

$$\frac{\delta \mathbf{V}_f}{\delta t} = \left.\frac{\delta \mathbf{V}_f}{\delta t}\right|_0 + \left.\frac{\partial(m_{11}\mathbf{F}_c+m_{12}\mathbf{M}_c)}{\partial \boldsymbol{\delta}}\right|_0 \Delta\boldsymbol{\delta}, \quad \frac{\delta \boldsymbol{\omega}_f}{\delta t} = \left.\frac{\delta \boldsymbol{\omega}_f}{\delta t}\right|_0 + \left.\frac{\partial(m_{21}\mathbf{F}_c+m_{22}\mathbf{M}_c)}{\partial \boldsymbol{\delta}}\right|_0 \Delta\boldsymbol{\delta} \tag{14}$$

The longitudinal acceleration $\dot{V}_x$ is unsuitable to be controlled in the INDI loop due to the low bandwidth of throttle δ_p. Also, V_x has marginal variations under vertical turbulence excitation, so throttle can be used to achieve V_x control in long time scale. The state vector $\mathbf{x}$ is then given by $\mathbf{x} = [V_y, V_z, p, q, r]^T$, and the control vector is $\boldsymbol{\delta} = [\delta_{a_s}, \delta_{a_a}, \delta_e, \delta_r]^T$. Define the control effectiveness matrix G as

$$[G_{5\times4}] = \begin{bmatrix} \left.\frac{\partial(m_{11}\mathbf{F}_c+m_{12}\mathbf{M}_c)}{\partial \boldsymbol{\delta}}\right|_0 \\ \left.\frac{\partial(m_{21}\mathbf{F}_c+m_{22}\mathbf{M}_c)}{\partial \boldsymbol{\delta}}\right|_0 \end{bmatrix}, \quad \left[\frac{\partial \mathbf{F}_c}{\partial \boldsymbol{\delta}}\right] = \begin{bmatrix} 0 & \frac{\partial F_y}{\partial \delta_{a_a}} & 0 & \frac{\partial F_y}{\partial \delta_r} \\ \frac{\partial F_z}{\partial \delta_{a_s}} & 0 & \frac{\partial F_z}{\partial \delta_e} & 0 \end{bmatrix}, \quad \left[\frac{\partial \mathbf{M}_c}{\partial \boldsymbol{\delta}}\right] = \begin{bmatrix} 0 & \frac{\partial M_x}{\partial \delta_{a_a}} & 0 & \frac{\partial M_x}{\partial \delta_r} \\ \frac{\partial M_y}{\partial \delta_{a_s}} & 0 & \frac{\partial M_y}{\partial \delta_e} & 0 \\ 0 & \frac{\partial M_z}{\partial \delta_{a_a}} & 0 & \frac{\partial M_z}{\partial \delta_r} \end{bmatrix} \tag{15}$$

Eq. (14) can then be written as

$$\dot{\mathbf{x}} = \dot{\mathbf{x}}_0 + G(\boldsymbol{\delta} - \boldsymbol{\delta}_0) \tag{16}$$

The control aim of this paper is GLA and passenger comfort improvement. Passengers feel motion via their vestibular system, which contains semi-circular canals measuring rotational accelerations $\dot{p}, \dot{q}, \dot{r}$ and otolith organ measuring the specific force. The specific force $\mathbf{A} = \frac{\mathbf{F}-\mathbf{F}_G}{m}$ is defined as the non-gravitational force per unit mass, which is actually a proper acceleration relative to free-fall. Accelerometers also measure the specific force. The onboard accelerometers measure the resultant force of lift L, drag D, side force C and thrust T per unit mass. Expressing $\mathbf{A}$ in body frame as

$$m\mathbf{A} = \begin{bmatrix} \cos\alpha\cos\beta & -\cos\alpha\sin\beta & -\sin\alpha \\ \sin\beta & \cos\beta & 0 \\ \sin\alpha\cos\beta & -\sin\alpha\sin\beta & \cos\alpha \end{bmatrix} \begin{bmatrix} -D \\ C \\ -L \end{bmatrix} + \begin{bmatrix} T \\ 0 \\ 0 \end{bmatrix} = \begin{bmatrix} T - D\cos\alpha\cos\beta - C\cos\alpha\sin\beta + L\sin\alpha \\ -D\sin\beta + C\cos\beta \\ -D\sin\alpha\cos\beta - C\sin\alpha\sin\beta - L\cos\alpha \end{bmatrix}$$

When β and α are small, $A_z \approx -\frac{L}{m}$, which is consistent with the load factor $n = \frac{L}{mg}$ in g unit used in aeroelasticity (The z axis directions defined in flight dynamics and aeroelasticity are opposite). $n_z = -A_z/g$ and $n_y = A_y/g$ will be referred to as vertical and lateral loads in this paper.

In summary, the controller should minimize the variation of the specific force $\Delta\mathbf{A} = \mathbf{A} - \mathbf{A}_*$, instead of $\dot{V}_y, \dot{V}_z$ nor $d\mathbf{V}_f/dt$. $\mathbf{A}_*$ is the nominal specific force. Recall Eq. (8), when the origin of the body frame $x_f y_f z_f$ is close to the c.g. ($\tilde{S} \approx 0$), the translational equation can be simplified as

$$\frac{d\mathbf{V}_f}{dt} = \frac{\delta \mathbf{V}_f}{\delta t} + \boldsymbol{\omega}_f \times \mathbf{V}_f = \frac{\mathbf{F}}{m} = \frac{\mathbf{F}-\mathbf{F}_G}{m} + \frac{\mathbf{F}_G}{m} = \mathbf{A} + \mathbf{g} \tag{17}$$

In order to minimize $\Delta\mathbf{A}$, the pseudo-control for $\dot{V}_y, \dot{V}_z$ can be designed as

$$\begin{aligned}\nu_{\dot{V}_y} &= (V_z\omega_x - V_x\omega_z + g\sin\phi\cos\theta)\big|_0 + A_{*_y}\\ \nu_{\dot{V}_z} &= (V_x\omega_y - V_y\omega_x + g\cos\phi\cos\theta)\big|_0 + A_{*_z}\end{aligned} \tag{18}$$

The pseudo-control for angular acceleration $\dot{p}, \dot{q}, \dot{r}$ is designed as $\boldsymbol{\nu}_\omega = \mathbf{0}$. The pseudo-control inputs for automatic flight control purposes will be designed in Section VI. Replacing $\dot{\mathbf{x}}$ by $\boldsymbol{\nu}$, the incremental control inputs are found by inverting Eq. (16) as

$$\boldsymbol{\delta} - \boldsymbol{\delta}_0 = (G^TG)^{-1}G^T(\boldsymbol{\nu} - \dot{\mathbf{x}}_0) = G^+(\boldsymbol{\nu} - \dot{\mathbf{x}}_0) \tag{19}$$

Since traditional aircraft configurations (only have rudder, ailerons and elevator) do not have direct side force control surfaces, the number of control variables (four) is less than the number of controlled states (five). The Moore-Penrose pseudoinverse G^+ is used in the present INDI control law, which leads to a least squares solution. Side force control is achieved indirectly by rudder and asymmetric aileron deflections. By doing this, it is found that the lateral acceleration $\dot{V}_y$ channel is sensitive to phase lags and time delays. When the rudder initially generates positive side forces, the accompanying negative yawing moments will cause positive sideslip angle β. Because the absolute value of the stability derivative (e.g. $C_{Y_\beta} = -0.553$ in current model) is larger than those of the control derivatives ($C_{Y_{\delta_r}} = 0.118, C_{Y_{\delta a_a}} = -0.0275$), the desired side forces will be counteracted soon. For conventional configuration aircraft, sufficiently fast measurements and control surface deflections are required to achieve direct lateral load control. Direct side force control surfaces (e.g. wing tip control surfaces) will provide more possibilities for controller design.

The pseudoinverse of control effectiveness matrix also automatically leads to control allocation, e.g., for pitch rate control, control commands are allocated to both elevator and symmetric ailerons according to their control effectiveness. This INDI GLA control law is independent of the state-related aerodynamic model, which increases its robustness.

B. Acceleration Measurements and Noise Filtering

The present INDI control law requires feedback of state derivatives, namely $\dot{\mathbf{x}} = [\dot{V}_y, \dot{V}_z, \dot{p}, \dot{q}, \dot{r}]^T$. $\dot{V}_y, \dot{V}_z$ can be obtained from an integrated inertial navigation system. Angular acceleration sensors do exist, but they are not common. Angular accelerations can also be reconstructed from a group of accelerometers.[11] This approach however requires the precise relative positions between accelerometers and is sensitive to structural vibrations. An alternative way is to calculate angular accelerations by numerically differentiating rate gyro measurements. In any case, the measurements will contain noise, biases and delays. Moreover, numerical differentiation will amplify high frequency noise.

In this paper, we add zero-mean Gaussian white noise on the output channels to simulate measurement noise. First order low-pass filters $H(s)$ are used to wash out high frequency noise. Other high order filters are also feasible. Angular accelerations are then calculated by numerically differentiating filtered rate gyro measurements. The entire INDI GLA control law structure is illustrated by Fig. 4, in which $A(s)$ represent the actuator dynamics.

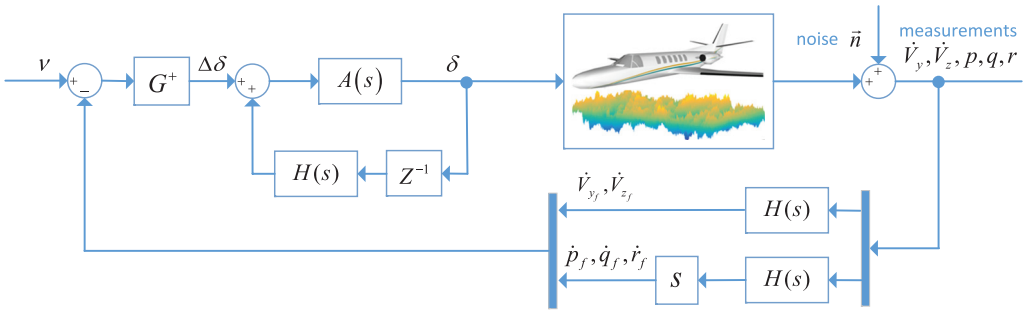

Figure 4. INDI gust load alleviation control law structure.

Filtering measurements will introduce phase lags, which degrade controller performance. By applying the same filters $H(s)$ on the input channels, synchronization between commands $\boldsymbol{\nu}$ and lagged measurements

$\dot{V}_{y_f}, \dot{V}_{z_f}, \dot{p}_f, \dot{q}_f, \dot{r}_f$ can be achieved.[18] However, the dynamic performance of the GLA control law is still influenced by actuator dynamics and measurement lags.[18]

C. Ride Comfort Evaluation

Jacobson[19] proposed a model to evaluate ride quality or comfort as

$$C_{trip} = \sum_{E=1}^{n} E^{3/4} C_E / \sum_{E=1}^{n} E^{3/4} \tag{20}$$

Here C_{trip} is the total comfort grade. E represents the sequentially numbered ride segment, C_E represent the corresponding comfort rating associated with turbulence, noise, temperature, seating, etc. Each ride comfort segment C_E is scaled from $1 = very\ comfortable$ to $7 = very\ uncomfortable$. The C_{mon} relates to turbulence/gust and is evaluated by the Root Mean Square (RMS) of vertical and lateral accelerations. As discussed in subsection A, these accelerations should be interpreted as the variations of the specific force $\Delta A_z,\ \Delta A_y$ (or the equivalent load variations $\Delta n_z = -\Delta A_z/g,\ \Delta n_y = \Delta A_y/g$). This can be illuminated by an example of a coordinated turn ($\beta = 0$), where the relative accelerations $\dot{V}_y, \dot{V}_z$ equal to zero, while the absolute acceleration $\frac{d\mathbf{V}_f}{dt}$ has components in both vertical and lateral body axes. However, passengers can only feel themselves become heavier. In other words, they feel the vertical load increases and the lateral load remains zero. Only the specific force can correctly reflect this phenomenon. The evaluation for C_{mon} is given by Eq. (21),[19] which will be used to evaluate the motion related comfort grade in section V.

$$C_{mon} = \begin{cases} 18.9\hat{\sigma}_{\Delta n_z} + 12.1\hat{\sigma}_{\Delta n_y}, & \hat{\sigma}_{\Delta n_z} \geq 1.6\hat{\sigma}_{\Delta n_y} \\ 1.62\hat{\sigma}_{\Delta n_z} + 38.9\hat{\sigma}_{\Delta n_y}, & \hat{\sigma}_{\Delta n_z} < 1.6\hat{\sigma}_{\Delta n_y} \end{cases} \tag{21}$$

V. INDI GLA Control Simulation Results

In this section, the time scale separation principle used in the INDI control will be verified. Following this, the INDI GLA control law will be tested by time domain simulations. The geometry parameters, lumped form inertia properties, and local aerodynamic coefficients of the aircraft all adopt data from Meirovitch's report.[2] The equilibrium point is chosen as a steady level flight with $H_* = 25000ft, V_{E_*} = 127m/s, Ma_* = 0.41$.

A. Validation of INDI Assumption

In Sec. IV, items related to $\Delta\mathbf{V}_f, \Delta\boldsymbol{\omega}_f, \Delta\boldsymbol{\theta}_f$ have been omitted from Eq. (13) based on the time scale separation principle. Although this principle has been explained analytically, the values of $\mathbf{K}_V, \mathbf{K}_\omega, \mathbf{K}_\theta, \mathbf{W}_V, \mathbf{W}_\omega, \mathbf{W}_\theta$ and $\mathbf{K}_\delta, \mathbf{W}_\delta$ will be numerically compared in this section.

1° step deflection commands are given to ailerons, elevator and rudder separately. In one incremental time step $\Delta t = 0.01s$ (with sampling frequency $f_s = 100Hz$), the values of $\mathbf{K}_V, \mathbf{K}_\omega, \mathbf{K}_\theta, \mathbf{W}_V, \mathbf{W}_\omega, \mathbf{W}_\theta, \mathbf{K}_\delta, \mathbf{W}_\delta$ are shown in Fig. 5.

It can be seen from Fig. 5 that in one incremental time step, $\mathbf{K}_\delta, \mathbf{W}_\delta$ are larger than $\mathbf{K}_V, \mathbf{K}_\omega, \mathbf{K}_\theta, \mathbf{W}_V, \mathbf{W}_\omega$, $\mathbf{W}_\theta$. For example, the 1° step deflection of symmetric ailerons δ_{a_s} leads to $K_{\delta_z} = -7m/s^2$ as direct effect. Its absolute value is 87 times larger than K_{V_z}, about 350 times larger than $|\mathbf{K}_\omega|$, and three orders of magnitude larger than $|\mathbf{K}_\theta|$. The 1° elevator step deflection results in $W_{\delta_y} = -0.12rad/s^2$ as direct effect, which is two orders of magnitude larger than $|\mathbf{W}_{\omega_y}|$, three orders of magnitude larger than $|\mathbf{W}_V|$ and five orders of magnitude larger than $|\mathbf{W}_\theta|$. In conclusion, the deflections of control surfaces lead to linear and angular acceleration variations as direct effects, other state-related items are at least two orders of magnitude smaller than control-related items. This further demonstrates the validity of the time scale separation principle used in INDI control laws.

B. INDI GLA Simulation Results

In this section, the INDI GLA control law derived in Section IV is applied on a quasi-rigid aircraft flying through both a continuous turbulence field (shown by Fig. 1) and a discrete gust field (shown by Fig. 2) to demonstrate its feasibility. Sampling frequencies of measurement noise are chosen as 100Hz, with

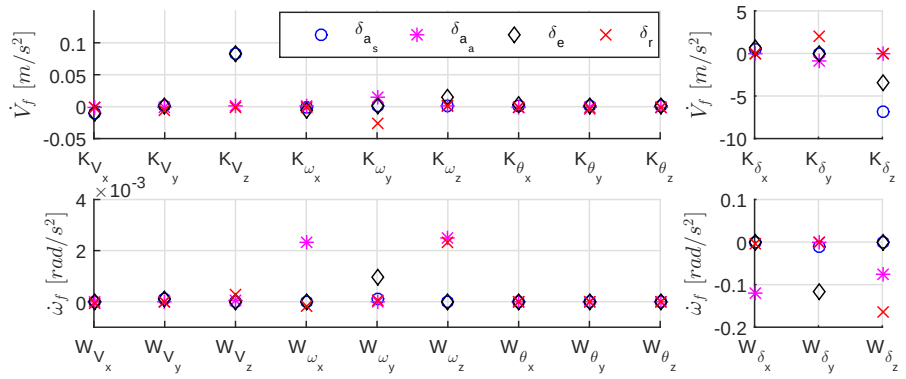

Figure 5. Values of $\mathbf{K}_V, \mathbf{K}_\omega, \mathbf{K}_\theta$ (top left), $\mathbf{K}_\delta$ (top right), $\mathbf{W}_V, \mathbf{W}_\omega, \mathbf{W}_\theta$ (bottom left) and $\mathbf{W}_\delta$ (bottom right) in Δt.

standard deviation $1 \times 10^{-4} rad/s$ for angular rate measurements, and $1 \times 10^{-3} m/s^2$ for linear acceleration measurements.

Figs. 6, 8, 7 illustrate the dynamic response of the aircraft flying through a 2D "1-cos" gust field (shown in Fig. 2), in which "open loop" means response without control, "ideal" represents INDI applied with ideal actuators, "actuator" refers to the INDI applied with actuator dynamics, "actuator+noise" means INDI applied considering both actuator dynamics and measurement noise. All the control surface actuator dynamics are modeled as first order systems with transfer function $A(s) = \frac{20}{s+20}$. The deflection limits of ailerons, elevator and rudder are $\pm 35°, \pm 25°, \pm 25°$ respectively. The cut-off frequency of all the filters is chosen as 16Hz to attenuate noise.

It can be seen from Figs. 6, 7 that the aircraft first encounters the symmetric gust $w_{g_1}(\lambda_x = \lambda_y = 100m, w_m = 5m/s)$ at $t = 0.7s$. Lateral states are undisturbed while the α increases 2.1° due to the upwash gust. The maximum magnitude of the incremental vertical load caused by the first gust is $|\Delta n_z| = 0.45g$ in the open loop response, and is alleviated to $|\Delta n_z| = 0.06g$ when INDI control is applied with ideal actuators. Actuator dynamics, however, introduce phase lags to the control surface deflections as shown in Fig. 8, which weakens the effectiveness of INDI control slightly. The asymmetric gust $w_{g_3}(\lambda_x = \lambda_y = 80m, w_m = 6m/s)$ causes rolling and yawing moments at $t = 10.8s$. The asymmetric gust induced sideslip angle β gives rise to lateral load as shown by Fig. 6. At $t = 14s$, the aircraft is exposed to a reversed asymmetric gust $w_{g_4}(\lambda_x = \lambda_y = 120m, w_m = 8m/s)$ with similar responses. Longitudinal states, such as q, α, are also influenced according to Fig. 7. The peak of the incremental lateral load has been reduced from $|\Delta n_y| = 0.033g$ in the open loop response to $|\Delta n_y| = 0.012g$ under INDI control.

The RMS as well as the peaks of incremental loads are summarized in Table 1. High frequency noise is successfully filtered by low-pass filters, so the inclusion of measurement noise has limited influence on aircraft response and GLA effectiveness.

Table 1. The RMS, peaks of incremental vertical, lateral loads and alleviation percentage.

	$\hat{\sigma}_{\Delta n_z}$ $[g]$		$\max \lvert\Delta n_z\rvert$ $[g]$		$\hat{\sigma}_{\Delta n_y}$ $[g]$		$\max \lvert\Delta n_y\rvert$ $[g]$	
Open loop	0.1134		0.4503		0.0086		0.0333	
INDI (ideal)	0.0112	90.1%	0.0579	87.2%	0.0016	81.3%	0.0118	64.6%
INDI (actuator)	0.0226	80.1%	0.1165	74.1%	0.0024	72.3%	0.0172	48.5%
INDI (actuator+noise)	0.0248	78.1%	0.1271	71.2%	0.0025	70.4%	0.0184	44.8%

Figs. 9, 10, 11 show the dynamic response of the aircraft flying through a 2D von Kármán turbulence field. In view of the high frequencies of the response signals, the cut-off frequency of all the filters $H(s)$ is chosen as 24Hz. Fig. 9 and Table 2 show the aircraft vertical and lateral loads measured on the origin of $x_f y_f z_f$. From these results it is obvious that the INDI control law reduces both vertical and lateral loads. When actuator dynamics and measurement noise are considered, the GLA effectiveness is attenuated, but the loads are still alleviated compared to the open loop response. Fig. 10 shows the aircraft state responses in the turbulence field. With the deflections of rudder and asymmetric ailerons, β is almost zero, so no outer

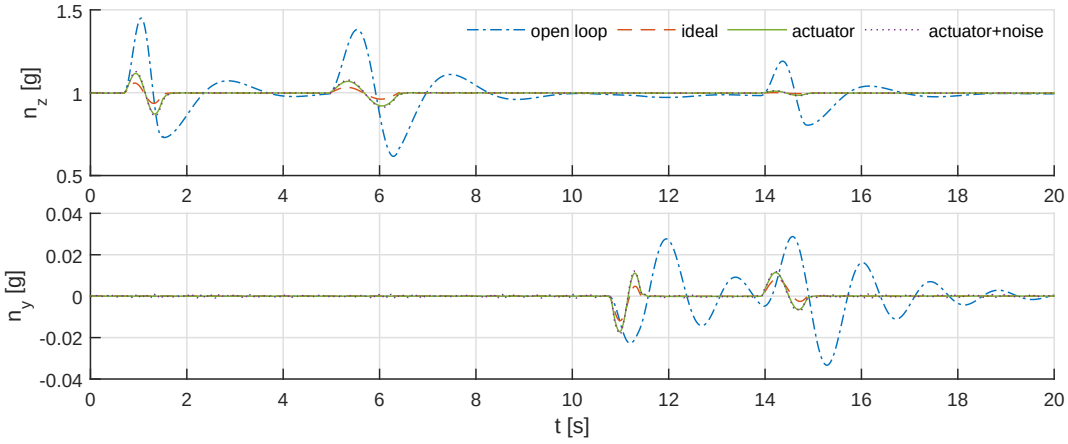

Figure 6. Aircraft load responses under 2D gust excitation.

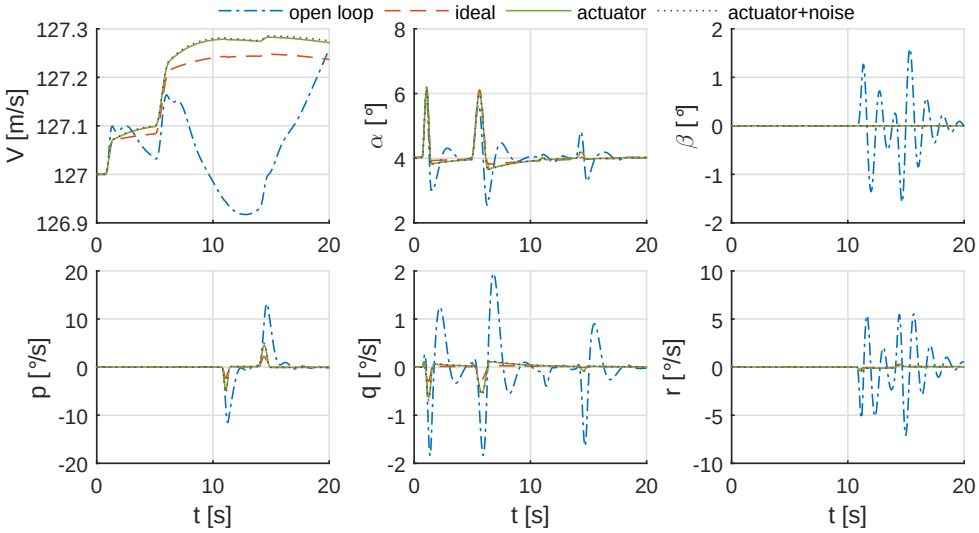

Figure 7. Aircraft state responses under 2D gust excitation.

loop sideslip angle control is needed. V_x is changing slowly, which can be easily controlled on a long time scale. As shown by Fig. 11, no control surface saturation occurs.

Table 2. The RMS of incremental vertical, lateral loads and alleviation percentage.

	$\hat{\sigma}_{\Delta n_z}$ $[g]$		$\hat{\sigma}_{\Delta n_y}$ $[g]$	
Open loop	0.1586		0.0063	
INDI (ideal actuator)	0.0282	82.2%	0.0043	31.8%
INDI (actuator dynamics)	0.0305	80.8%	0.0056	11.1%
INDI (actuator+noise)	0.0330	79.2%	0.0058	7.2%

Eq. (21) is used to evaluate the motion related comfort grade. As illustrated in Fig. 12, under turbulence excitation, the ride quality grade has been improved from $C = 4$, *neutral* to $C = 1$, *very comfortable*, while it has been improved from $C = 3$, *somewhat comfortable* to $C = 1$, *very comfortable* under gust excitation.

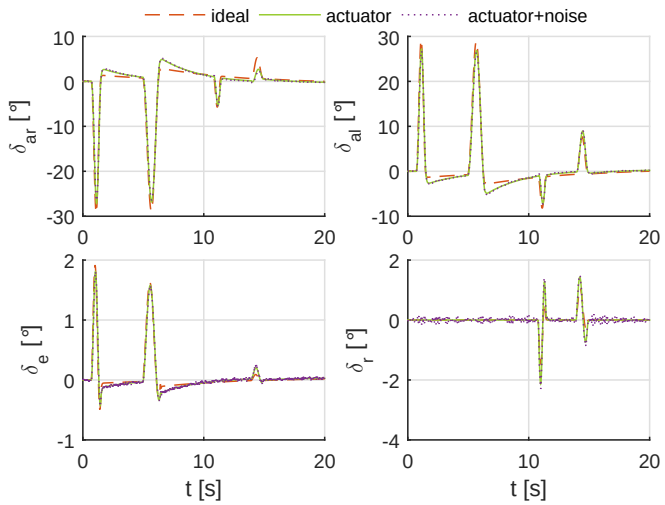

Figure 8. Control surface deflections using INDI under 2D gust excitation.

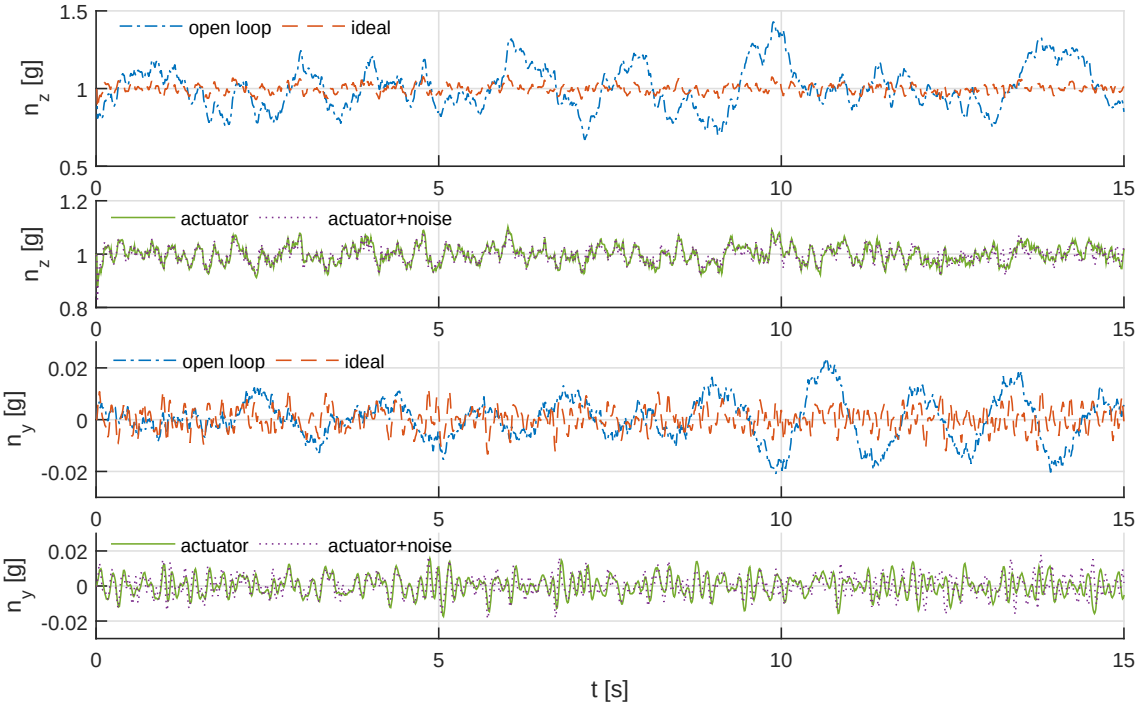

Figure 9. Aircraft load responses under 2D turbulence excitation.

VI. Comparison with LQR

A classical method to stabilize a system and alleviate loads is LQR/LQG control.[2,4] The coupled nonlinear high order system dynamics are generally linearized at a trim point, and then model reduction methods[20] are applied for the convenience of linear controller design. For quasi-rigid aircraft, system states can be easily measured by onboard sensors, so LQR control is adequate. For flexible aircraft, however, most of the elastic states can only be observed from outputs, so LQG control, which is essentially a combination of LQR control and Kalman filter, is more suitable.

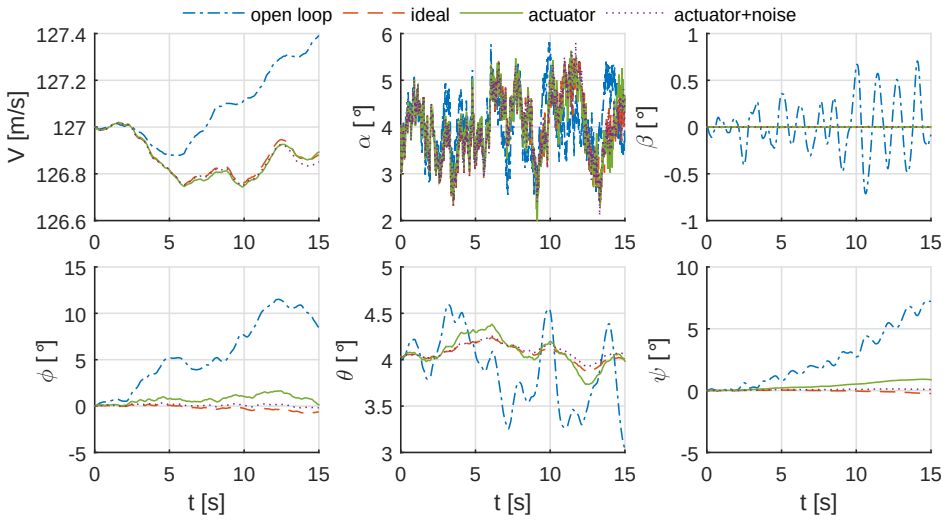

Figure 10. Aircraft state responses under 2D turbulence excitation.

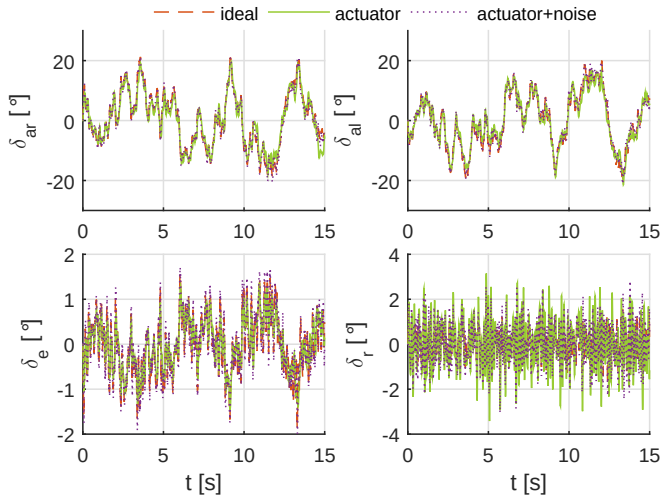

Figure 11. Control surface deflections using INDI under 2D turbulence excitation.

A. LQR GLA Control Law

For a linear system $\dot{\boldsymbol{x}} = A\boldsymbol{x} + B\boldsymbol{u}$, an LQR controller is designed with the following cost function:

$$J = \frac{1}{2}\int_0^{t_f} (\boldsymbol{x}^T Q\boldsymbol{x} + \boldsymbol{u}^T R\boldsymbol{u})dt \tag{22}$$

The Q and R matrices are tuned using Bryson's rule.[21] By solving the algebraic Riccati equation $A^T P + PA + Q - PBR^{-1}B^T P = 0$, the optimal control is given by $\boldsymbol{u} = -K\boldsymbol{x} = -R^{-1}B^T P\boldsymbol{x}$. The actuator dynamics ($A(s) = \frac{20}{s+20}$) are also included in the linear model, which introduce four open loop poles at -20.

By using LQR control, the loads are indirectly alleviated by minimizing the states. Since LQR is a linear proportional controller, there is no new state introduced by the controller. If a better GLA performance is desired, the values in the Q matrix should be larger, and the closed-loop eigenvalues will be assigned more negative in the complex plane to resist disturbance. Two different settings of Q and R matrices are tested, and the resulting closed-loop eigenvalues are given in Table 3.

Considering a quasi-rigid aircraft flying through a 2D von Kármán turbulence field with different controllers, the system responses as well as the RMS of loads are given by Figs. 13, 14, 15 and Table 4. For the

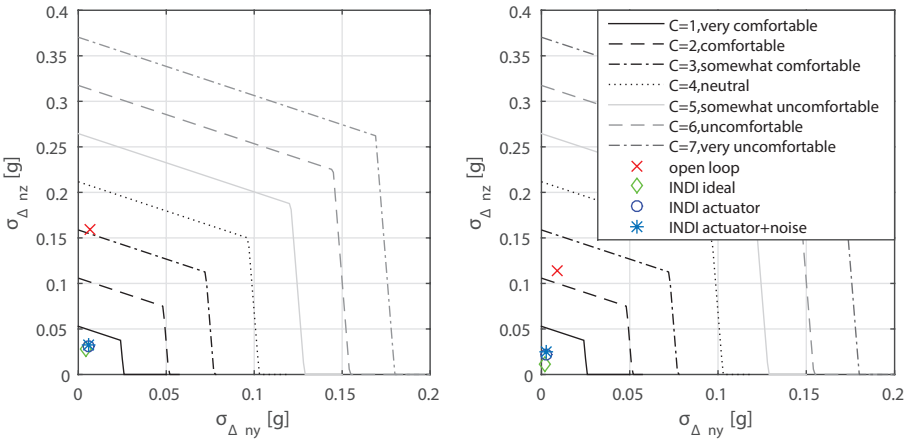

Figure 12. Ride comfort grades under turbulence (left) and gust (right) excitation.

Table 3. The closed-loop eigenvalues using different Q, R settings.

Open loop	No.1 (Q_1, R_1)	No.2 (Q_2, R_2)
-0.00650 ± 0.120i	-0.0792	-0.0793
-0.0138	-0.0167 ± 0.0720i	-0.0209 ± 0.0686i
-0.659 ± 4.46i	-19.5 ± 13.3i	-21.9 ± 16.6i
-0.975 ± 2.33i	-21.8	-23.7
-2.23	-45.6 ± 76.1i	-46.4 ± 77.2i
-20.0 (four)	-48.9 ± 67.4i	-55.1 ± 68.8i
	-60.0	-60.2
	-88.2	-89.4

LQR controllers, the more negative the closed-loop eigenvalues are, the better disturbance rejection will be achieved. Also, as shown in Table 4 and Fig. 14, under similar RMS of aileron deflections, the INDI control has improved vertical GLA performance compared to LQR No.4.

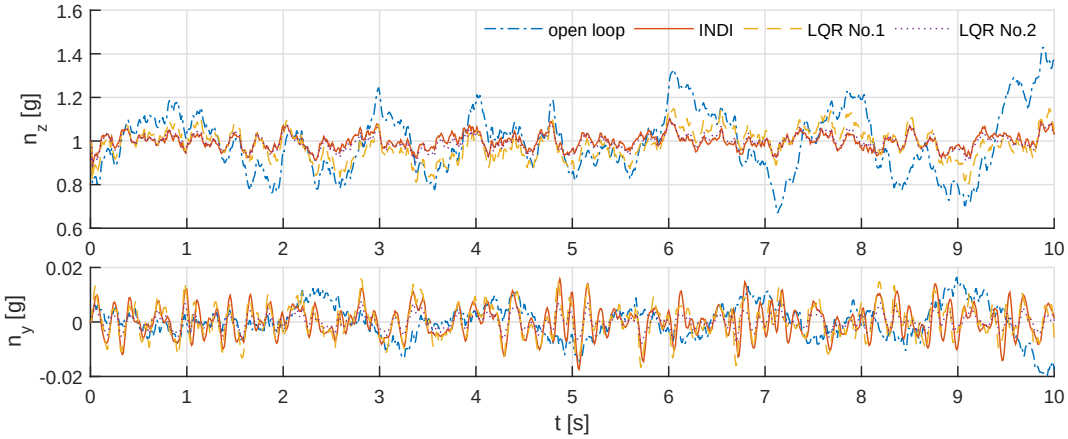

Figure 13. INDI/LQR GLA effectiveness under 2D turbulence excitation.

Table 4. The RMS of incremental loads and aileron deflections using INDI/LQR control.

	$\hat{\sigma}_{\Delta n_z}$ $[g]$		$\hat{\sigma}_{\Delta n_y}$ $[g]$	$\hat{\sigma}_{\delta_{ar}}$ $[rad]$	$\hat{\sigma}_{\delta_{al}}$ $[rad]$
Open loop	0.1586		0.0063	0	0
LQR No.1	0.0702	55.7%	0.0058	0.0967	0.0894
LQR No.2	0.0355	75.7%	0.0028	0.1341	0.1266
INDI(with actuator)	0.0305	80.8%	0.0056	0.1375	0.1298

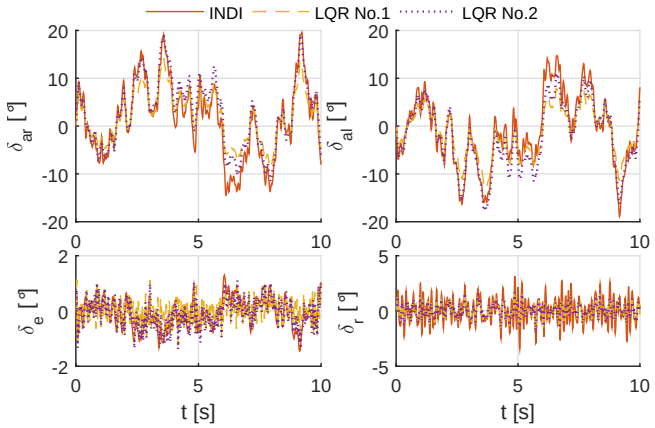

Figure 14. Control surface deflections using INDI/LQR under 2D turbulence excitation.

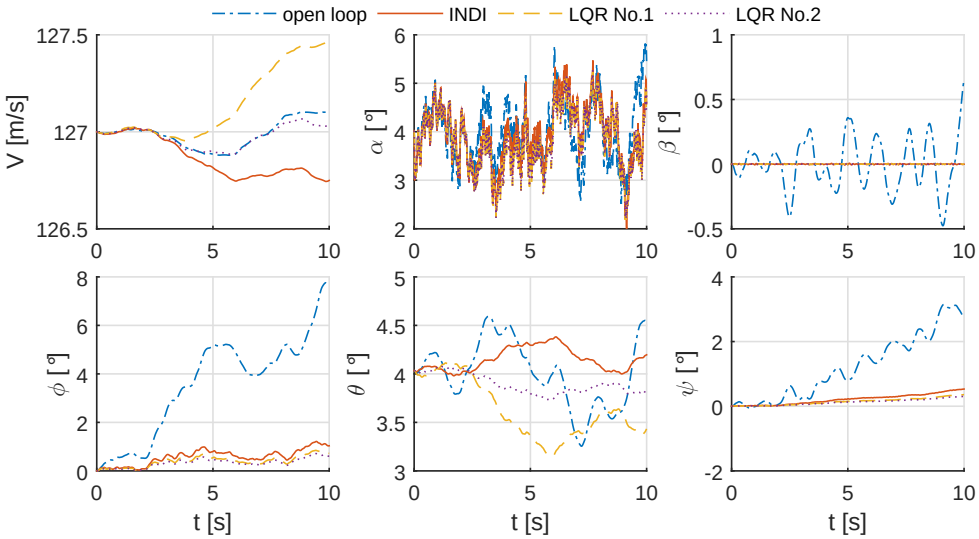

Figure 15. State responses using INDI/LQR control under 2D turbulence excitation.

B. Tracking Performance Comparison

Apart from GLA, the aircraft should be able to track the pilot commands. Tracking tasks include flight path tracking, attitude control, etc. In this section, a pitch angle command tracking task is considered.

For LQR control, with the closed-loop eigenvalues moving to the left, the system dynamics becomes faster. However, the closed-loop gain will reduce and consequently bring increasing steady-state error. This is essentially a trade off between stability and maneuverability. In order to find a balance between load alleviation and command tracking performance, a multi-objective cost function is needed.[3] The system is augmented with the integration of the tracking error $x_e = \int_0^t (\theta - \theta_{ref})dt$, and the augmented model plant

can be expressed as

$$\begin{bmatrix} \dot{\boldsymbol{x}} \\ \dot{x}_e \end{bmatrix} = \begin{bmatrix} A & 0 \\ C_e & 0 \end{bmatrix} \begin{bmatrix} \boldsymbol{x} \\ x_e \end{bmatrix} + \begin{bmatrix} B \\ 0 \end{bmatrix} \boldsymbol{u} + \begin{bmatrix} 0 \\ -\theta_{ref} \end{bmatrix}, \quad \theta = C_e \boldsymbol{x} \tag{23}$$

The corresponding cost function is given by $J = \frac{1}{2}\int_0^{t_f} (\boldsymbol{x}^T Q \boldsymbol{x} + \boldsymbol{u}^T R \boldsymbol{u} + x_e^T Q_e x_e) dt$, with Q_e representing the weighting matrix for tracking error. Three different LQR designs are tested and the resulting eigenvalues are given in Table 5. These three controllers are then applied to a nonlinear quasi-rigid aircraft model, under a 5 degrees θ_{ref} block command, the state responses are shown in Figs. 16 and 18. Only the right aileron deflection is shown in Fig. 17, since during the θ_{ref} tracking task, ailerons are used symmetrically.

Table 5. The closed-loop eigenvalues using different Q, R settings.

Open loop	No.3 (Q_3, R_3, Q_{e3})	No.4 (Q_4, R_4, Q_{e4})	No.5 (Q_5, R_5, Q_{e5})
-0.00650 ± 0.120i	-0.0185	-0.0184	-0.0135
-0.0138	-0.0309	-0.0793	-0.0218
-0.659 ± 4.46i	-0.678 ± 0.677i	-0.639 ± 0.643i	-0.765 ± 0.513i
-0.975 ± 2.33i	-2.02	-21.9 ± 16.6i	-1.27 ± 4.60i
-2.23	-19.2 ± 29.7i	-23.7	-1.53 ± 2.68i
-20.0 (four)	-20.0 (two)	-46.4 ± 77.2i	-2.20
	-20.9 ± 33.8i	-55.1 ± 68.8i	-20.0 (four)
	-37.8	-60.2	
	-42.1	-89.4	

As shown in Fig. 16, using all the three controllers, the system is able to track the θ_{ref} block command. Most of the closed-loop poles of LQR No.3 and No.4 are more negative compared to LQR No.5. Consequently, more control effort should be paid to change the states under LQR No.3 and No.4 control, which can be illustrated by Figs. 17 and 18. By contrast, system controlled by LQR No.5 has better maneuverability, marginal aileron deflections and halved elevator deflection are required to follow the command. However, as can be deduced, the system using LQR No.5 control is more sensitive to disturbance. This is proved by Fig. 19, in which the tracking performance deteriorates and the RMS of load increases using LQR No.5 control. LQR No.4 controller can better resist the disturbance, though more control energy is required as shown in Fig. 20.

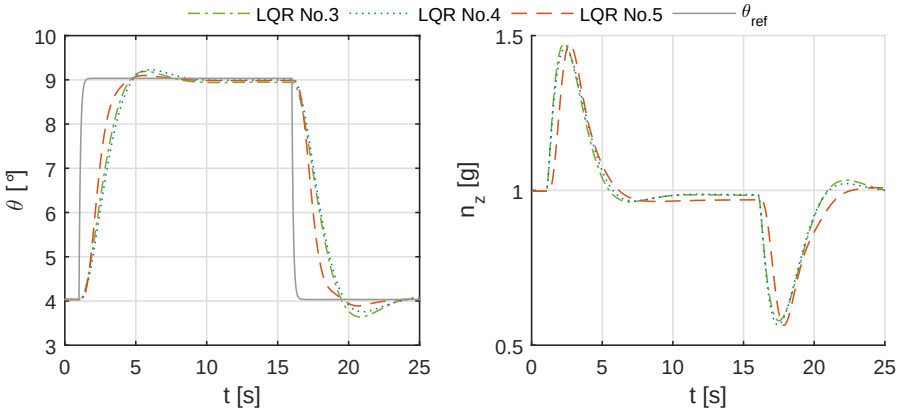

Figure 16. The θ and n_z responses using LQR control under θ_{ref} tracking command.

Since the linear system dynamics are only determined by the closed-loop eigenvalue positions, the tracking and GLA performance are tied together in the LQR control. Among all the five LQR controllers, if a better GLA performance is required, LQR No.2 can be a desirable controller. To follow the commands given by the pilot, maneuverability has priority, so LQR No.5 is more suitable. If both tracking performance and GLA are considered, LQR No.4 is a reasonable choice, though more control effort would be sacrificed. The controller

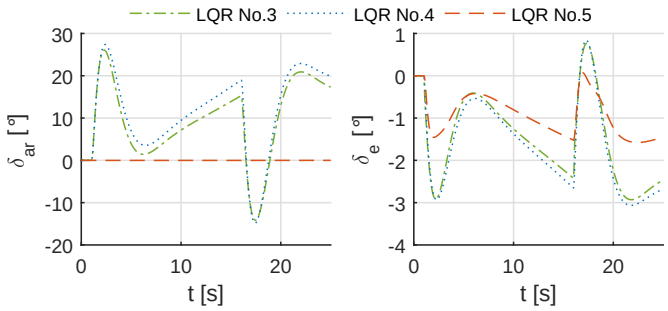

Figure 17. Control surface deflections using LQR control under θ_{ref} tracking command.

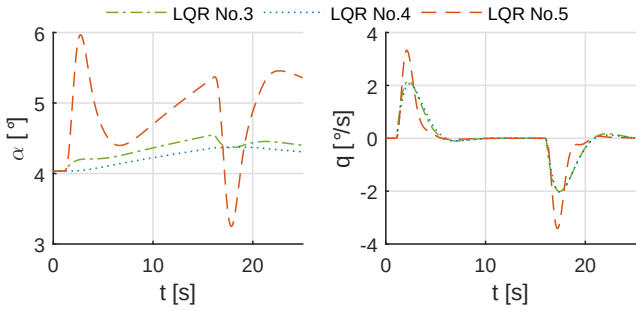

Figure 18. State responses using LQR control under θ_{ref} tracking command.

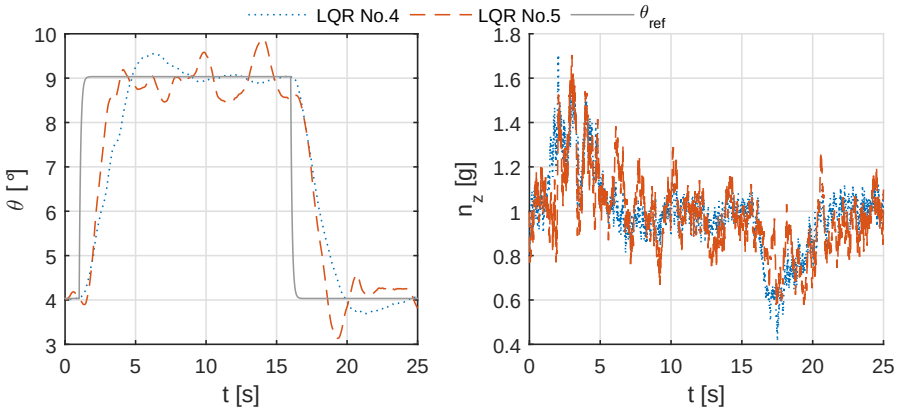

Figure 19. The θ and n_z responses using LQR control in a turbulence field.

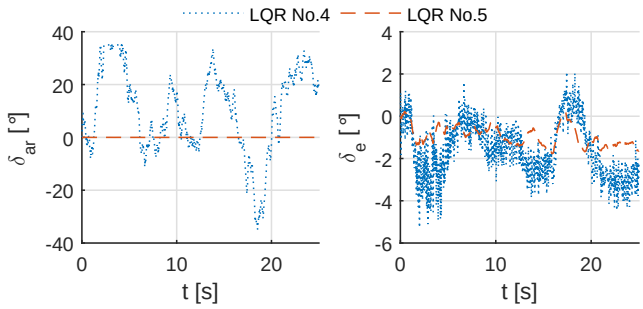

Figure 20. Control surface deflections using LQR control in a turbulence field.

parameters of LQR should be tuned based on different tasks and a trade off should be made between GLA, tracking performance and required control energy.

The INDI GLA control law designed in Sec. IV can be easily extended to an automatic flight control law. By using INDI GLA control in the inner loop, the nonlinear cross couplings of states are all canceled, leading to the linear system dynamics $\dot{\mathbf{x}} = \dot{\mathbf{x}}_0 + GG^+(\boldsymbol{\nu} - \dot{\mathbf{x}}_0)$. If the control effectiveness matrix G is a full rank square matrix, the system dynamics are given as unified $\dot{\mathbf{x}} = \boldsymbol{\nu}$, and all the state control channels are fully decoupled. The lateral dynamics are coupled together for the G matrix used in this paper, because asymmetric ailerons and rudder need to control three states V_y, p, r. On the other hand, symmetric ailerons and elevator can achieve a decoupled control of V_z and q. This means the aircraft is able to simultaneously track independent $\nu_{\dot{V}_z}$ and $\nu_{\dot{q}}$ commands.

Because all the nonlinearities have been canceled by using INDI GLA, the virtual control for angular accelerations can be designed by an outer loop linear proportional controller. Taking the attitude control task for example, the control law structure is given by Fig. 21, in which the angular acceleration virtual control is $\boldsymbol{\nu}_\omega = [\nu_{\dot{p}}, \nu_{\dot{q}}, \nu_{\dot{r}}] = K_{\omega_f}(\boldsymbol{\omega}_{com} - \boldsymbol{\omega}_f)$, $K_{\omega_f} = diag[K_p, K_q, K_r]$. The angular rate command $\boldsymbol{\omega}_{com}$ is given by the outer loop attitude controller using Nonlinear Dynamic Inversion (NDI). Defining the virtual control as $\boldsymbol{\nu}_{att} = \dot{\boldsymbol{\theta}}_f$, the control command for angular rates can be calculated by

$$\begin{aligned} \boldsymbol{y}_{att} &= \boldsymbol{\theta}_f, \qquad \dot{\boldsymbol{y}}_{att} = \dot{\boldsymbol{\theta}}_f = E_f^{-1}\boldsymbol{\omega}_f \\ \boldsymbol{\nu}_{att} &= \dot{\boldsymbol{\theta}}_f, \qquad \boldsymbol{\omega}_{com} = E_f \boldsymbol{\nu}_{att} \end{aligned} \tag{24}$$

Since the kinematic matrix $E_f(\theta, \phi)$ only depends on Euler angles which can normally be measured accurately, NDI is used here. The virtual control $\boldsymbol{\nu}_{att}$ can again be generated by a proportional controller $\boldsymbol{\nu}_{att} = K_{\theta_f}(\boldsymbol{\theta}_{com} - \boldsymbol{\theta}_f)$, $K_{\theta_f} = diag[K_\psi, K_\theta, K_\phi]$. Using this control structure, the transfer function of pitch angle tracking is given by Eq. (25). If the actuator dynamics is included and modeled as a first order system, the closed-loop dynamics in the pitch channel is represented by a third-order system. The gain matrices $K_{\theta_f}, K_{\omega_f}$ can be designed to obtain the desired natural frequencies, damping ratios and to ensure closed-loop stability.

$$\frac{\theta}{\theta_{com}} = \frac{K_q K_\theta}{s^2 + K_q s + K_q K_\theta} \tag{25}$$

One feature of the proposed INDI flight control system is that the $\dot{V}_z$ and $\dot{q}$ control channels are fully

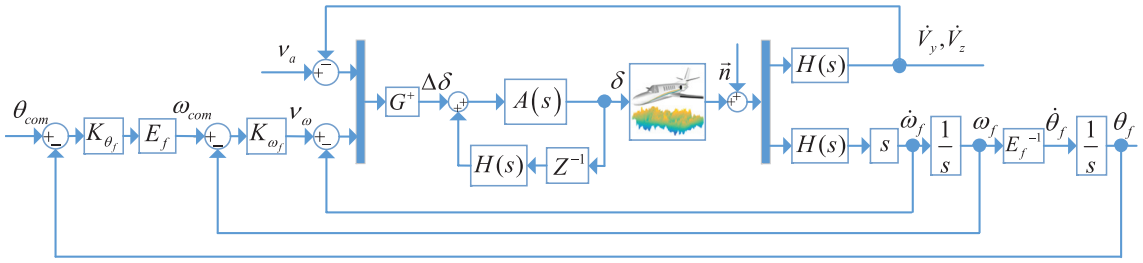

Figure 21. INDI attitude control law structure.

decoupled. If the pseudo-control $\nu_{\dot{V}_z}$ is used to control load as given by Eq. (18), then the desired vertical load profile n_{z_*} (or A_{z_*}) can be achieved without influencing the tracking performance in the $\dot{q}$ control channel. If the n_{z_*} is designed to be the natural and undisturbed load response during maneuvers, control surfaces will only alleviate the incremental load caused by the disturbances. Assuming the flight path angle γ is small and the lift is only proportional to α, the natural load response profile during longitudinal maneuvers can be estimated from the aircraft dynamic equations as

$$\begin{aligned} V\dot{\gamma} &= \frac{L}{m} - g\cos\gamma \approx \Delta n_z g, \quad \dot{\gamma} = q - \Delta\dot{\alpha} \\ \Delta n_z &= K_\alpha \Delta\alpha = \frac{q_\infty S C_{L_\alpha}}{mg}\Delta\alpha = \frac{V}{g}\frac{1}{\frac{V}{K_\alpha g}s + 1}q \end{aligned} \tag{26}$$

The n_{z_*} profile can also be designed for maneuver load alleviation (MLA) purposes, and the tracking performance will not be affected. In order to illustrate this feature, INDI controllers with different n_{z_*} profiles are

compared to the LQR control with poles position No.4 during a pitch angle tracking task. The parameters of INDI are tuned to be $K_\theta = 0.7, K_q = 2.5$ with the results shown in Figs. 22 and 23.

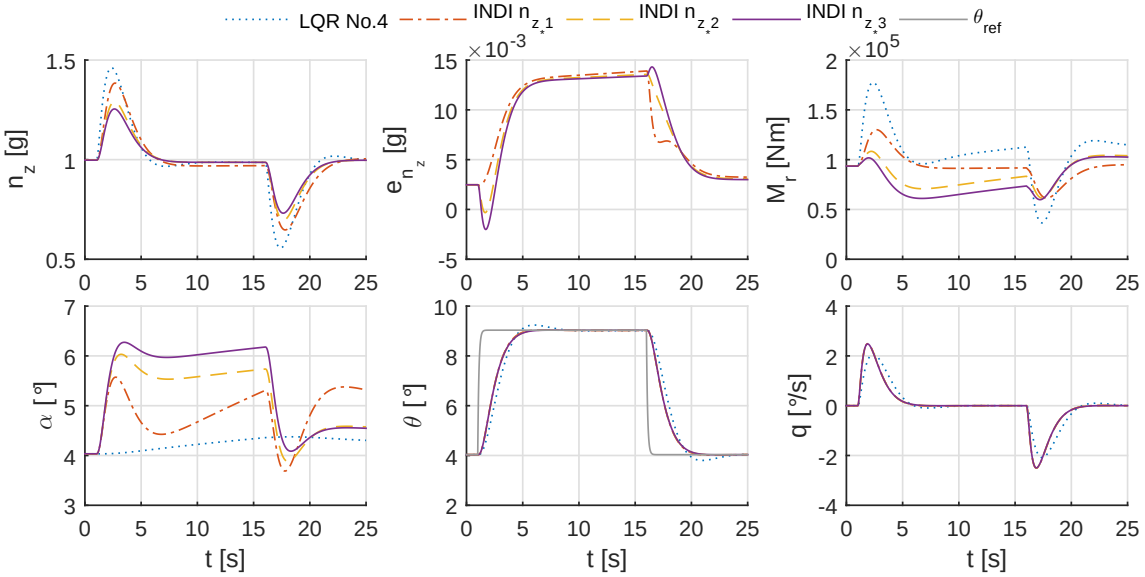

Figure 22. The n_z, wing root bending moment and responses using INDI/LQR control.

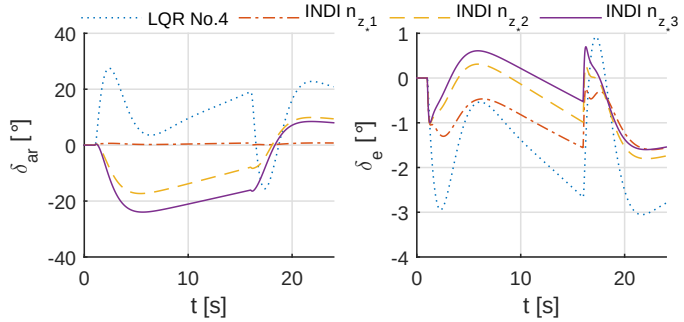

Figure 23. Control surface deflections using INDI/LQR control under θ_{ref} command.

As shown in Fig. 22, using INDI control, for any given n_{z_*} profile, the θ and q responses remain the same, and the tracking is faster than the LQR control. The tracking errors $e_{n_z} = n_z - n_{z_*}$ are all within 1.5% of the n_{z_*} references. The load command for INDI n_{z_*1} is the natural and undisturbed maneuver load calculated by Eq. (26), so the ailerons do not contribute to the MLA as shown in Fig. 23. The INDI controller with load profile n_{z_*3} is designed to alleviate maneuver load. By redistributing the lift, the RMS of wing root bending moment M_r using n_{z_*3} has been alleviated by 27.1% compared to LQR control. The maximum value of M_r has also been reduced by 42.0%.

Furthermore, using the n_{z_*1} profile as the load command, the INDI control is able to alleviate the gust load during maneuvers. As illustrated in Fig. 24, in a turbulence field, the tracking performance of INDI is hardly disturbed, and the load has smaller variations compared to the LQR control. Besides, under LQR No.4 control, the aileron saturated from $t = 2s$ to $t = 4s$ as shown in Fig. 25, while the RMS of both the aileron and elevator deflections are lower under INDI control.

C. Robustness to Aerodynamic Uncertainties

Based on preceding derivations, it can be seen that the only model knowledge required by the INDI control is the control effectiveness matrix G, while LQR controller depends on accurate knowledge of the entire

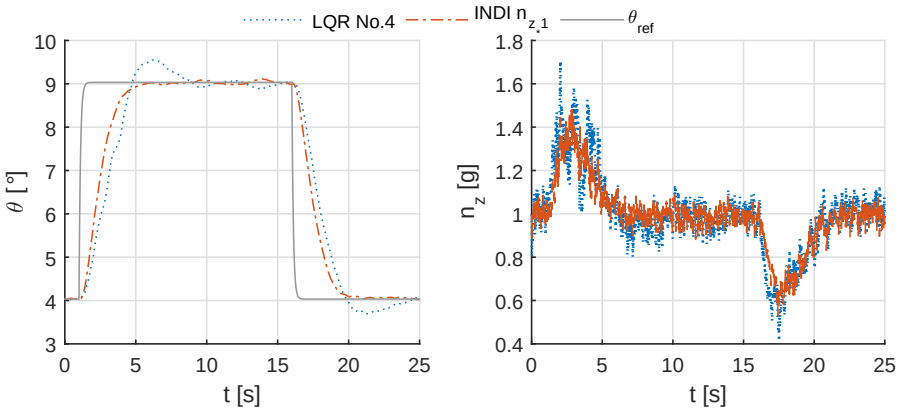

Figure 24. The θ and n_z responses using INDI/LQR control in a turbulence field.

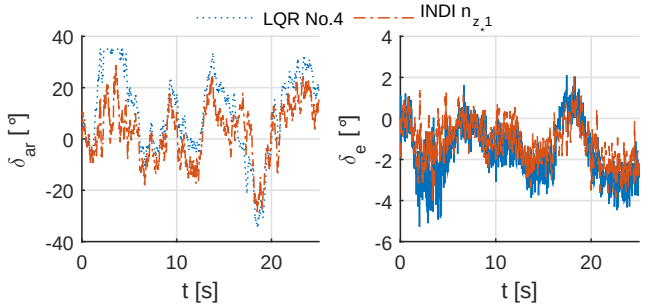

Figure 25. Control surface deflections using INDI/LQR control in a turbulence field.

aerodynamic model. When the sampling frequency is high, the uncertainties in control effectiveness matrix G do not significantly influence the INDI control.[12]

The current aerodynamic model of the quasi-rigid aircraft is based on quasi-steady strip theory. The aircraft model contains k components, namely the fuselage (f), engine pylon (p), wing (w), tail (t), elevator (ele), ailerons (ail), and rudder (ru). Each aircraft component is divided into n_k strips and the corresponding local lift coefficients are given at one preselected trim point. In reality, the aerodynamic model is uncertain and varies with time. Therefore, the model is extended by lift coefficient uncertainties, which are assumed to be normally distributed real numbers given as

$$\mathbf{\Delta}_k := \Delta \in \mathbb{R} | \Delta = N(0, \sigma_k^2), \quad \sigma_k = \frac{0.3}{n_k} \sum_{i=1}^{i=n_k} C_{l_i}, \quad k = f, p, w, t, ele, ail, ru. \tag{27}$$

For each component k, the mean value of uncertainty is zero and the standard deviation σ_k is chosen as 30% of the nominal average lift coefficient value of this component. The robustness of LQR control with eigenvalue position No.2 and INDI control are compared during a GLA task. The aircraft with aerodynamic model uncertainties is flying through a von Kármán turbulence field using pre-designed LQR and INDI control with an observation time of 20 seconds. Fig. 26 presents a Monte-Carlo simulation results containing 1000 samples of the uncertain aerodynamic models. It can be seen that the interquartile range (IQR) of the RMS of vertical load $\hat{\sigma}_{n_z}$ using INDI control is smaller than that of the LQR control, which supports the better robustness performance of the INDI control.

In addition, this INDI controller is also robust to the variation of c.g. position. The nonlinear simulation model adopts data from Meirovitch's report,[2] in which the c.g. deviates from the body axes origin. However, the pseudo-control designed by Eq. (18) does not use this model information.

In summary, from different perspectives, the INDI control and LQR/LQG control can be compared as

1. Task-specific control: The cost function of LQR/LQG control targets a specific task. For different tasks, GLA, pitch angle control, roll angle control, and flight path control, the cost function should be

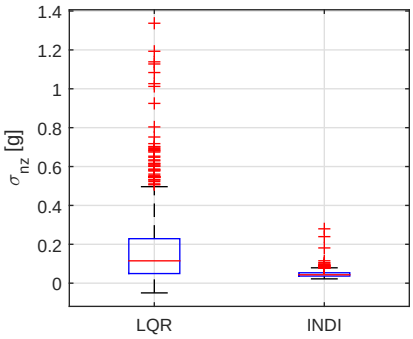

Figure 26. Box plot of a Monte-Carlo simulation of an aircraft using LQR/INDI GLA control subject to aerodynamic model uncertainties.

redesigned and the Q, R matrices should be re-tuned. On the other hand, INDI control is less task-specific. The virtual control $\boldsymbol{\nu_\omega}$ can be designed in a classical linear cascaded way, which is convenient for switching between different automatic flight control modes.

2. Global control and robustness: INDI is a nonlinear control method which ensures global performance. Once selected, in principle, the control parameters $K_{\theta_f}, K_{\omega_f}$ do not need adjustments. When the control derivatives deviate from the nominal values, parameter tuning or adaptation may be needed. INDI is also more robust to aerodynamic model uncertainties. As a linear controller, if multiple flight conditions are considered, gain scheduling is required for LQR/LQG control. The parameter tuning and interpolation process of gain scheduling method can be tedious.

3. GLA performance: By directly controlling the accelerations, INDI control can more effectively alleviate the gust loads during maneuvers compared to the LQR control.

4. Tracking performance and GLA/MLA: The tracking and GLA/MLA performances are tied together in LQR control. If a better maneuverability is desired, the load alleviation performance will degrade. On the contrary, the tracking performance of INDI depends on the outer loop virtual control $\boldsymbol{\nu_\omega}$ design, which is decoupled from load alleviation. This decoupling ensures the priority of pilot commands, and the desirable load profile n_{z_*} can be designed to alleviate gust/menevuer load.

VII. Conclusions

In this paper, a non-cascaded Incremental Nonlinear Dynamic Inversion (INDI) gust load alleviation (GLA) control law is proposed to alleviate gust loads and to improve ride quality. Direct lift control is applied using coordinated deflections of ailerons and elevator. By inverting the control effectiveness matrix, the control allocation is achieved for a traditional aircraft configuration. The time scale separation principle used in INDI is verified both analytically and numerically. The time domain simulations of a quasi-rigid aircraft flying through various spatial turbulence and gust fields demonstrate the feasibility of the proposed INDI GLA control law.

The INDI GLA control law is further extended to an INDI automatic flight control law. Since the nonlinear cross couplings of states are canceled by INDI, the outer loop automatic flight control law can be designed using linear proportional control in a classical cascaded way. The desirable vertical load profile n_{z_*} can be designed to alleviate the gust/maneuver load, and the load alleviation will not influence the flight control performance. This INDI flight control law is verified during a pitch angle command tracking problem, showing that the desired tracking performance can be achieved while alleviating the gust load.

The tracking performance is decoupled from load alleviation using INDI control, while they are tied together in LQR control. The cost function of LQR/LQG targets a specific task while INDI control can conveniently switch between different automatic flight control modes. As a nonlinear controller, INDI ensures global performance. In addition, a Monte-Carlo simulation demonstrates the better robustness of INDI control to aerodynamic model uncertainties.

In the future, the INDI control method is also a promising approach for flexible aircraft gust load alleviation problems.

References

[1]Waszak, M. R. and Schmidt, D. K., "Flight Dynamics of Aeroelastic Vehicles," *Journal of Aircraft*, Vol. 25, No. 6, 1988, pp. 563–571.

[2]Meirovitch, L. and Tuzcu, I., "Integrated Approach to the Dynamics and Control of Maneuvering Flexible Aircraft," Tech. rep., NASA/CR-2003-211748, June 2003.

[3]Nguyen, N. and Tal, E., "A Multi-Objective Flight Control Approach for Performance Adaptive Aeroelastic Wing," *56th AIAA/ASCE/AHS/ASC Structures, Structural Dynamics, and Materials Conference*, Reston, Virginia, 2015.

[4]Nguyen, N. T., Swei, S., and Ting, E., "Adaptive Linear Quadratic Gaussian Optimal Control Modification for Flutter Suppression of Adaptive Wing," *AIAA Infotech@Aerospace*, Reston, Virginia, 2015, pp. 1–23.

[5]Moulin, B. and Karpel, M., "Gust Loads Alleviation Using Special Control Surfaces," *Journal of Aircraft*, Vol. 44, No. 1, 2007, pp. 17–25.

[6]Aouf, N., Boulet, B., and Botez, R., "H2 and H infinity Optimal Gust Load Alleviation for a Flexible Aircraft," *Proceedings of the 2000 American Control Conference. ACC*, Vol. 46, IEEE, 2000, pp. 1872–1876 vol.3.

[7]Zeng, J., Moulin, B., de Callafon, R., and Brenner, M. J., "Adaptive Feedforward Control for Gust Load Alleviation," *Journal of Guidance, Control, and Dynamics*, Vol. 33, No. 3, 2010, pp. 862–872.

[8]Haghighat, S., T. Liu, H. H., and R. A. Martins, J. R., "Model-Predictive Gust Load Alleviation Controller for a Highly Flexible Aircraft," *Journal of Guidance, Control, and Dynamics*, Vol. 35, No. 6, 2012, pp. 1751–1766.

[9]Regan, C. and C. Jutte, "Survey of Applications of Active Control Technology for Gust Alleviation and New Challenges for Lighter-weight Aircraft," Tech. Rep. NASA/TM-2012-216008, April 2012.

[10]Sieberling, S., Chu, Q. P., and Mulder, J. A., "Robust Flight Control Using Incremental Nonlinear Dynamic Inversion and Angular Acceleration Prediction," *Journal of Guidance, Control, and Dynamics*, Vol. 33, No. 6, 2010, pp. 1732–1742.

[11]Bacon, B. and Ostroff, A., "Reconfigurable Flight Control Using Nonlinear Dynamic Inversion with a Special Accelerometer Implementation," *AIAA Guidance, Navigation, and Control Conference and Exhibit*, Reston, Virigina, 2000, pp. 1–15.

[12]Simplício, P., Pavel, M., van Kampen, E., and Chu, Q. P., "An Acceleration Measurements-Based Approach for Helicopter Nonlinear Flight Control Using Incremental Nonlinear Dynamic Inversion," *Control Engineering Practice*, Vol. 21, No. 8, 2013, pp. 1065–1077.

[13]Roland, S., *Meteorology for Scientists and Engineers*, Brooks/Cole, 2000.

[14]Etkin, B., *Dynamics of Atmospheric Flight*, Dover Publications, Toronto, 2005.

[15]Robinson, P. A. and Reidt, L. D., "Modeling of Turbulence and Downbursts for Flight Simulators," *Journal of Aircraft*, Vol. 27, No. 8, 1989, pp. 700–707.

[16]Etkin, B., "Turbulent Wind and Its Effect on Flight," *Journal of Aircraft*, Vol. 18, No. 5, 1981, pp. 327–345.

[17]Mohammadi-Amin, M., Ghadiri, B., Abdalla, M. M., Haddadpour, H., and De Breuker, R., "Continuous-time State-space Unsteady Aerodynamic Modeling Based on Boundary Element Method," *Engineering Analysis with Boundary Elements*, Vol. 36, No. 5, 2012, pp. 789–798.

[18]Smeur, E. J. J., Chu, Q. P., and de Croon, G. C. H. E., "Adaptive Incremental Nonlinear Dynamic Inversion for Attitude Control of Micro Air Vehicles," *Journal of Guidance, Control, and Dynamics*, Vol. 39, No. 3, 2016, pp. 450–461.

[19]Jacobson, I. D., Kuhlthau, A. R., Richards, L. G., and Conner, D. W., "Passenger Ride Quality in Transport Aircraft," *Journal of Aircraft*, Vol. 15, No. 11, 1978, pp. 724–730.

[20]Newman, B. and Schmidt, D. K., "Numerical and Literal Aeroelastic-Vehicle-Model Reduction for Feedback-Control Synthesis," *Journal of Guidance Control and Dynamics*, Vol. 14, No. 5, 1991, pp. 943–953.

[21]Franklin, G. F., Powell, J. D., and Emami-Naeini, A., *Feedback control of dynamic systems*, Vol. 2, Addison-Wesley Reading, 1994.